

Study of the System Response Analysis for the Eddy Current Test Crack Assessment on SS 316 Metal Arc Welding Joints

Rubijanto Juni Pribadi ^{a,b}, Rusnaldy ^{a,*}, Gunawan Dwi Haryadi ^a

^a Mechanical Engineering, Universitas Diponegoro, Jl. Prof. Jacub Rais - Tembalang, Semarang, 50275, Indonesia

^b Universitas Muhammadiyah Semarang, Jl. Kedung Mundu No. 18. Semarang, 50273, Indonesia

Corresponding author: *rubijanto.jp@unimus.ac.id,

Abstract— In modern industry, accurately assessing metal coupling by welding is critical. Given its reliability and other advantages, the eddy current test (ECT) is essential and commonly used in metal processing, especially welding. The classical ECT assesses the presence of discontinuities in the structure by monitoring the change in the probe's impedance. According to the wireless power transfer (WPT) theory, ECT members will exchange power wirelessly through mutual induction determined by inductance, capacitance, and resistance (LCR). The cracks will affect the mutual induction in the ECT's power exchange. Since LCRs are impedance components, the crack in the target will affect the system's mutual induction, as it did to the impedance in the classical ECT. This study applies the WPT model of ECT, implements system response analysis to assess cracks, and compares the results with classical ECT. The test piece is a metal arc-welded joint on SS 316 with an implanted notch on the welded joint to simulate the crack. A series of initial tests were performed to ensure the test piece was defects-free. Simulation and a frequency scan were performed to acquire a safe measurement. The result was that both the classical ECT and the system's response analysis successfully assessed the presence of cracks with excellent agreement. The system's response analysis yields a more rapid result than classical ECT.

Keywords— System's response; eddy current; non-destructive test; welded joint; cracks.

Manuscript received 10 Mar. 2024; revised 1 Apr. 2024; accepted 1 May. 2024. Date of publication 30 Jun. 2024.
IJASEIT is licensed under a Creative Commons Attribution-Share Alike 4.0 International License.



I. INTRODUCTION

In modern industry, welded joints are commonly used to couple various metals. Several tests must be performed to evaluate the structure's performance against mechanical failure, including tensile and compressive tests categorized by their load, such as operational loads for standard service and overloads for exceptional service. Various modes of failure can occur to the structure at multiple stages, such as the operational and fabrication stages [1]. A common issue in a structure's welded joints is fatigue failure, caused by the joint's inability to cope with the loads applied to it. Tests, either destructive or non-destructive, must be performed to produce a safe structure.

ECT has been developed for non-destructive test purposes in many applications, including defect tests, plate thickness tests, coating thickness tests, material identification, and monitoring damage to metal structures caused by heat. Researchers have made many modifications to ECT by varying the frequency (single, multiple, pulsed, or swept) and the geometry of the probe. The increase in sensitivity of the

measurement and the ability to determine the geometry become the common goals in the eddy current research subject [2].

The testing of the ECT is divided into experimental and simulation stages for confirmation and validation tools [3], [4]. The computer is utilized to perform the finite element-based simulation. Testing of electromagnetic analysis and methods (TEAM) dictates that the experimental system for the ECT test must consist of at least three components. The injection component includes an oscillator or current generator and an injection coil, the detection component consists of a detection coil, and an indicator device displays the signal quantity received by the detection system in the ECT network [5]–[7]. In ECT, a crack in a conductive structure will produce a higher amplitude than a location without cracks [8]. The impedance of the target or assessed location affects the signal level in ECT. The impedance of the probe alters when the probe is in the vicinity of the crack. By definition, impedance is the total resistance given by the target to changes in current injected from the injection system and consists of resistance, inductance, and capacitance.

Inductance occurs because a magnetic field changes the voltage in an electric circuit. The changes in impedance will alter the amplitude of the signals. In ECT, the presence of cracks in the metallic structure will produce a higher amplitude compared to the one without cracks.

According to WPT theory, the ECT system's components, consisting of an injector, detector, and target, will exchange power wirelessly when a stimulus frequency is applied. Based on this analogy, ECT can be analyzed using WPT theory, which models the transfer of energy through the LCR network between the coils [9]–[11]. In WPT, power exchange between the members is calculated with the system's response at a certain point of the system. The point above is the point where the output of the system is being monitored. The system's impedance determines the system's response when injected with a specific amount of stimulus power and is used mathematically to analyze the system's response.

The development of ECT is increasing along with technological advances. Various techniques and methods were applied in ECT experiments, with the common goal of achieving rapid and reliable results. However, a system's response analysis had never been implemented to assess flaws in metallic structure as the ECT did by monitoring the change in impedance when the ECT probe swept a target.

This study will analyze the step-unit response of the power exchange in the ECT system using the WPT model and compare the results with classical ECT. The target is a metal arc-welded joint of SS 316. According to ASTM's requirements for the ECT standard for the qualification of the specimen, we implanted a crack in the welded joint using an electric discharge machine (EDM). The crack is implanted transversely on the welded joint at a predetermined location on the specimen, i.e., in the middle. When assessing the crack, we study the probe's response and compare it to the classic ECT as dictated by the TEAM's benchmark for solving Problem No. 15 about a multiturn coil above a conductive plate in the halfspace [10]

According to the TEAM's benchmark, the experiment is performed by measuring the change in the probe's impedance as the probe sweeps along a certain path of the testpiece. When the target is a welded joint, the probe will sweep along the welded joint and pass through the implanted crack. The probe sweep begins when the center of the probe is above the perimeter of the testpiece and ends when the center of the probe reaches the perimeter on the other side of the testpiece. Things to consider about ECT on welded joints are that the roughness of the welded joint caused by the welding bead generates very little noise to signal and can be neglected [12].

When modeled as WPT, ECT works by inducing coupling between the injection coil, the detection coil, and the target. The power transfer works by equalizing the resonance between those three [13]–[17]. The detection coil detects an eddy current that floats on the target's surface, opposing the injected current's direction [18]. By inducing a time-varying time signal through the injector, mutual induction between the members of the ECT is possible.

There are several topologies in the WPT modeling to configure the LCR circuit. Series-series (SS) LCR topology is the most common used to perform the electrical network calculation [19]. In the S-S topology, reactance between

members can be limited, minimize resistivity loss, and obtain proportional impedance [16], [20]–[22].

Fig. 1 shows the illustration of the coils in ECT probe's when applied to a target.

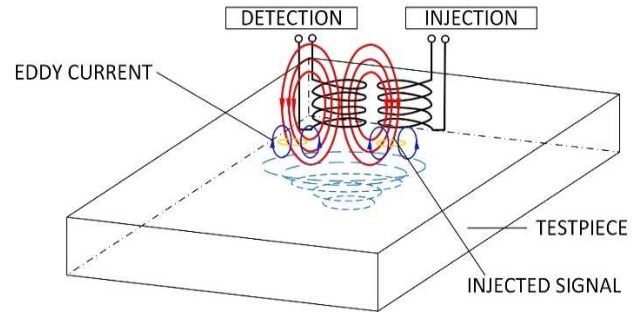


Fig. 1 Illustration of eddy currents on a target

To model the classic ECT according to the TEAM's benchmark, the Dodds and Deeds model about the impedance in the coils above a conductive plate in half space with thickness c is applied to the model, as shown in Fig. 2 [23], [24]. Figure 2 depicts a probe characterized by its coil thickness d , inner diameter r_1 , outer diameter r_2 , and a lift-off distance of h mm above the conductive target. The probe will exhibit impedances denoted as Z^{in} and Z^{SC} .

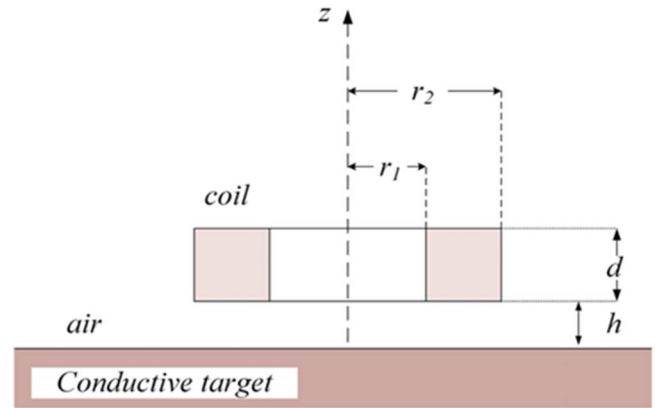


Fig. 2 Dodd and Deeds model for calculating the probe's impedance

$$Z^{in}(j\omega) = 2j\omega\pi\mu_0 n_c^2 \sum_{i=1}^{\infty} \text{Int}^2(r_1, r_2, \lambda) \times \frac{2[(\lambda_1 d - 1 + \exp(-\lambda_1 d))]}{[(\lambda_1 b)J_0(\lambda_1 b)]^2 \lambda_1^5} \quad (1)$$

$$Z^{SC}(j\omega) = 2j\omega\pi\mu_0 n_c^2 \sum_{i=1}^{\infty} \text{Int}^2(r_1, r_2, \lambda) \times \frac{2[\exp(\lambda_1 h) - \exp(-\lambda_1(h+d))]^2}{[(\lambda_1 b)J_0(\lambda_1 b)]^2 \lambda_1^5} \times \frac{\lambda_1 \mu_r - u_i}{\lambda_1 \mu_r + u_i} \quad (2)$$

where Z^{in} and Z^{SC} are the impedance of the probe in the air and the impedance of the probe when it is applied to the conductive target. λ is the eigen value of the eigen function, b is the distance between truncated boundary and the symmetry axis, and μ_0, μ_2 , and μ_r are the permeability of air, measurement target, and the relative permeability of measurement target.

By implementing constant amplitude alternating current (CAAC), as done by Luloff et al., the impedance of the probe can be considered as [25]:

$$I = \frac{V(\omega)}{R + j\omega L} \quad (3)$$

where I is the current, V is the voltage, R is the resistance, L is the inductive reactance, and ω is the angular frequency $\omega = 2\pi f$.

As shown in (3), the impedance acquired from (1) and (2) should only contain inductive reactance and no capacitive reactance since the presence of capacitive reactance leads to biased measurement. This is because of the nature of capacitance that stores energy, causing dissonance in the injected signal [10].

To determine the system's response, unit-step response analysis is instrumental to acquire information about how the system will respond to a unit-step input. The system is modeled in the frequency domain to perform the system response analysis. The unit step input is used to assess the system's response, as represented in the unit step response diagram. In the unit-step response diagram, an analysis is made about the rise time, the time required for the response to reach its final value. The illustration of the rise time in the second-order unit step response diagram can be seen in Fig. 3.

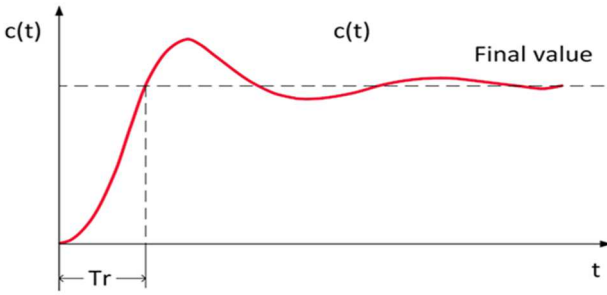


Fig. 3 Rise time (t_r) in the unit step's response

II. MATERIALS AND METHODS

ECT is performed by monitoring the change in impedance when the probe is near the discontinuity of the testpiece. The experiment changed the probe's impedance relative to the probe's distance to the crack. The impedance diagram will be represented for the result. We compared the system's response experiment result, represented by the rise time, with the results from the classical ECT. The data were taken every 5 mm probe displacement, and since the length of the testpiece is 100 mm, the total data is 20. The results are represented by the impedance diagrams and the probe's position relative to the location of the crack in the target. This research compares the results of classical ECT and the system's response analysis.

To model the ECT system for the step input response analysis, we use Fig. 4, where each component of the ECT consists of an injector, detector, and target. Subscripts I, D, and T are used for the injector, detector, and target. LCR represents inductors, capacitors, and resistors. By implementing the S-S topology for the configuration, the point of interest for measurement in this model is the R_T .

From Fig. 4, M_{DI} is the mutual induction between the detection of the injection coil and the target. R_L is the point of

interest in acquiring the system's response. The output of the system's response will be calculated using the transfer function to obtain the system's unit-step response. From the unit step response, we can acquire the rise time of the system's step response.

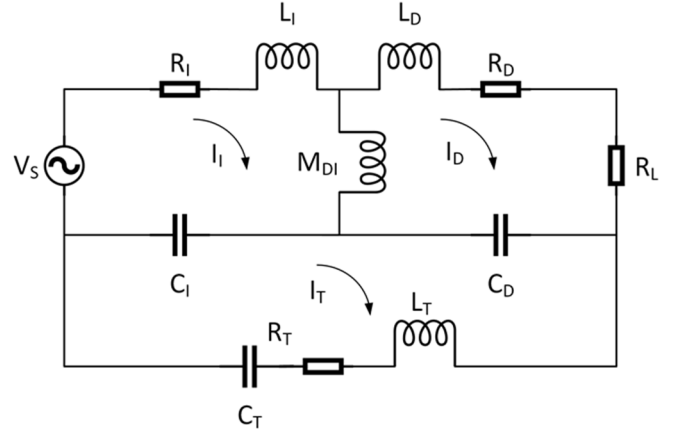


Fig. 4 The equivalent circuit for ECT

From Fig. 4, with circuit theory, by simply using the Kirchoff voltage law (KVL) and Kirchoff current law (KCL) for the equivalent circuit of ECT, we can get the following:

$$\begin{cases} V_{in} = (R_I + j\omega L_I)I_1 - j\omega M_{DI}I_D - \frac{1}{j\omega C_I}I_T \\ 0 = -j\omega M_{DI}I_2 + \\ (j\omega M_{DI} + R_D + R_L + \frac{1}{j\omega C_D}I_D) - \frac{1}{j\omega C_D}I_T \\ 0 = -\frac{1}{j\omega C_I}I_1 - \frac{1}{j\omega C_D}I_D + \\ (\frac{1}{j\omega C_I} + \frac{1}{j\omega C_D} + j\omega L_T + R_T)I_T \end{cases} \quad (4)$$

The transfer function of the KVL equation is

$$T(s) = \frac{\begin{bmatrix} R_I + j\omega M_{DI} & -j\omega M_{DI} & \frac{1}{j\omega C_I} \\ -j\omega M_{DI} & j\omega M_{DI} + R_D & 0 \\ \frac{1}{j\omega C_I} & \frac{1}{j\omega C_D} & 0 \end{bmatrix}}{(\Delta)(V_{in})} \quad (5)$$

Where

$$\Delta = \begin{bmatrix} R_I + j\omega M_{DI} & -j\omega M_{DI} & \frac{1}{j\omega C_I} \\ \frac{1}{j\omega C_I} & j\omega M_{DI} + R_D & 0 \\ -j\omega M_{DI} & +R_L + \frac{1}{j\omega C_D} & \frac{1}{j\omega C_I} \\ \frac{1}{j\omega C_I} & \frac{1}{j\omega C_D} & \frac{1}{j\omega C_I} + j\omega L_T + R_T \end{bmatrix} \quad (6)$$

The test piece is a SMAW-welded joint that couples two SS 316 metal plates with a size of 50x50 and a thickness of 4 mm. The geometric parameters of the test piece after the welding process are listed in Table 1. The welded joint is a square butt weld, with geometric parameters illustrated in Fig. 5.

TABLE I
THE TESTPIECE'S GEOMETRIC PARAMETERS

Parameter	Dimension (mm)
y	96.66
x	98.54
z	1.20
w	6
h	1.15

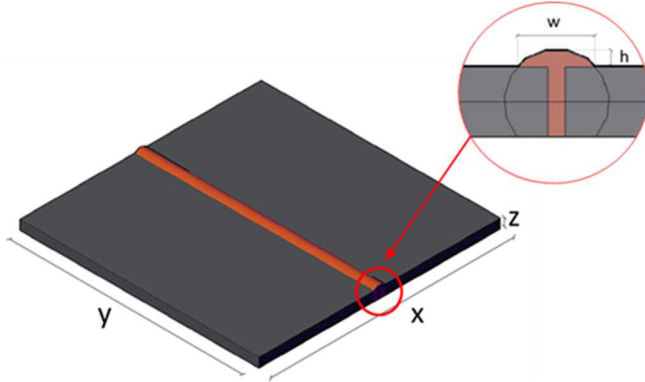


Fig. 5 The testpiece's geometric parameters

In the fabrication process of the testpiece, the welding process is done in one pass, the welding current is 60 A, and a certified welder carried out the welding process. A composition test is also done on the testpiece, ensuring that the testpiece's material is SS 316. A welding quality stage is carried out to ensure that the testpiece's surface is flawless. The testpiece's welded connection was inspected by a certified welding inspector. A certified radiographer performed a radiography test as part of the subsurface evaluation process. Immediate corrections were done if a flaw was found in the welded joint. AWS standards are followed in the correction of any existing weld flaws. The radiography test result is shown in Fig. 6.

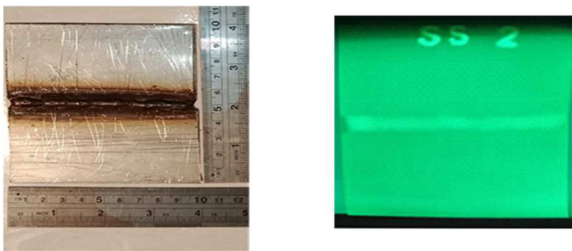


Fig. 6 The testpiece and its radiographic test results.

The next step is to implant the notch to simulate the crack in the testpiece. An electric discharge machine (EDM) is used to implant the cracks. The crack location is exactly in the middle of the length of the welded joint. The crack is implanted perpendicular to the longitudinal direction of the welded joint. Considering that the thickness of the testpiece is 1.2 mm, the implant's depths are 0.5 mm and 1 mm.. The experimental setup in this experiment is shown in Fig. 7.

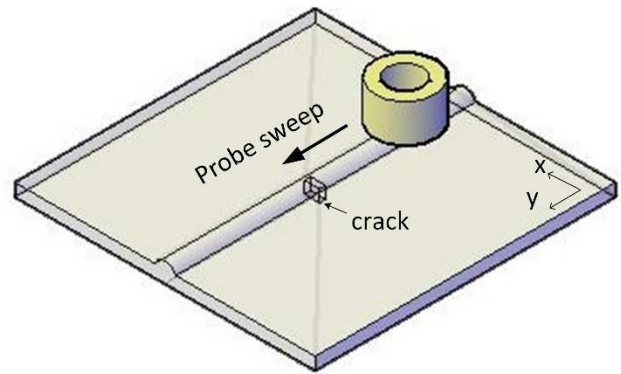


Fig. 7 The experimental setup

We fabricate a planar probe to perform the probing in the experiment. According to the design, Fig. 8 shows both the probe design and the fabricated probe. Like PCB etching, the copper geometry is etched on the Kapton sheet. The geometry was made using computer-aided drawing. The etched copper is the detection coil. A bar-shaped PCB was etched and then cut to perform the injection. A casing was made to cover the probe.. The casing is made of nylon that is turned to form a bobbin. Electric terminals in the coil and the injection bar allow for external connection. The injection bar is connected to the wave generator, and the detection coil is connected to an oscilloscope. Table 2 outlines the probe's parameters.

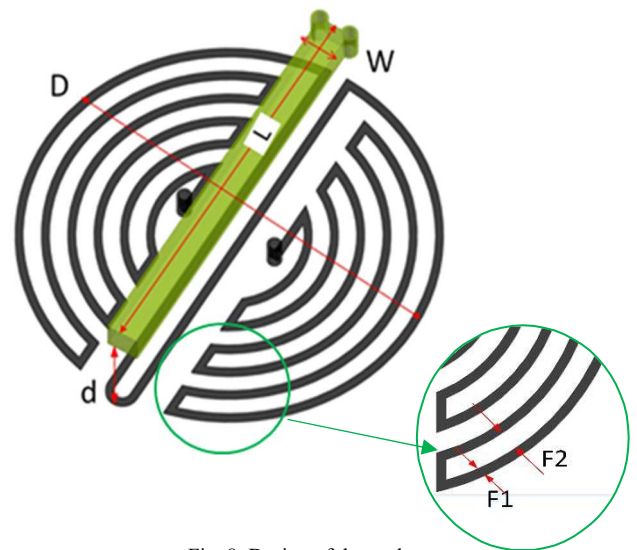


Fig. 8 Design of the probe

TABLE II
GEOMETRIC PARAMETERS OF THE PLANAR PROBE DESIGN

Parameter	Dimension (mm)	
W	Injection trace's width	2
L	Injection trace's length	25
D	The probe's external dimensions	25
d	The injection trace's distance to the detection coil	15
F1	The width of the winding of the detection coil	1.5
F2	Clearance of the detection coil	2

Before being used for probing, the probe is tested with a frequency scan, where the probe is injected with a stimulus frequency ranging from 100 Hz to 1 MHz. When a frequency test is performed, the probe has to be free from any conductive material that may interfere with it. To obtain such a condition, the probe was hung, and then the stimulus frequency was injected into the probe through the wave generator, and the detection coil would record the probe's response through the oscilloscope. The data for the frequency scan is 20 data points plotted in stimulus frequency versus the inductance of the probe. To validate the probe's performance, an FEM simulation was also performed to map the magnetic flux distribution of the probe.

Monitoring the change in the probe's impedance was done when the probe swept the test piece along the welded joint by carefully dislocating the test piece in y direction while the probe was hanging still. The measurements were taken at the 5 mm step of the probe displacement. The measurement is done when the center of the probe is above the location where the measurement is required. The sweep starts when the probe's center is above the target's perimeter and ends on the perimeter on the other side of the testpiece. The classic ECT data representations are the impedance diagram and the change in impedance versus the probe's position. Figure 9 shows the experimental configuration used in this study to perform the ECT.

The same probe-swept technique was also used to acquire the step input response of the ECT system. The probe also swept along the target, and the change in the LCR was monitored and then calculated to acquire the system's response at the same measurement points as in the classical ECT experiment done in this study. The results of the classical ECT will then be compared with the step input response data results.

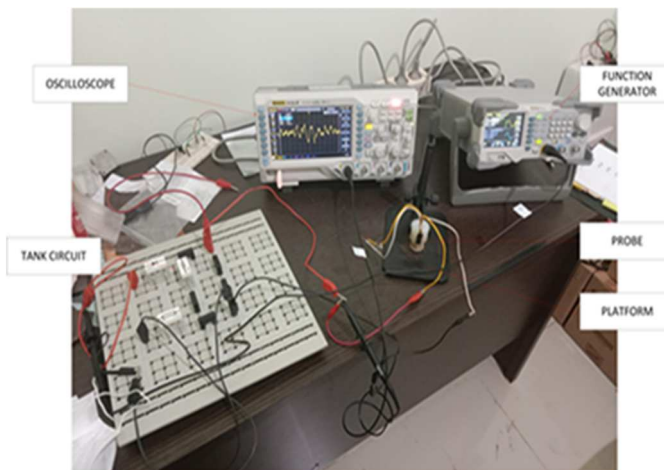


Fig. 9 The experimental setup for ECT

III. RESULT AND DISCUSSION

The results of the frequency scan experiment for the safe measurement are shown in Fig. 10. There are two results in Fig. 10. The first one is the response of the injection coil, marked by red dots. This result is typical in the one-coil system, where a single coil serves as a detector and an injection. The second line is the detection coil's response to the injection coil's injected stimulus frequency. The second

line, marked by black dots, is used when the multi-coil or detection coil separates from the injection coil. So, we can say that both lines represent the detected signal. When the single coil is used as an injector, it detects the signal simultaneously. Another scenario involves the injector delivering the signal injection while another handles the detection, as in the multi-coil system in the graph [26] [27].

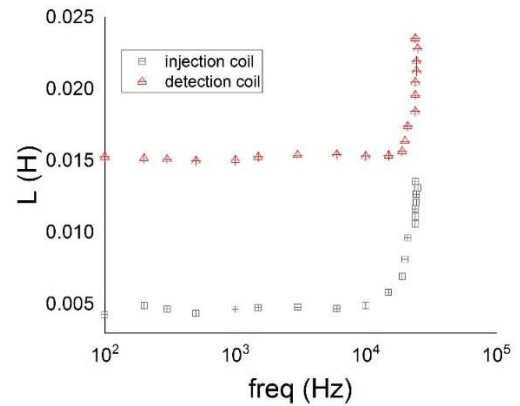


Fig. 10 The result of frequency scan experiment

The result shows that when we use the 2-coil mode, where the detection coil is applied, it will respond with a higher inductance than the single coil. This indicates that the two coils will result in high-sensitivity probing. The detection coils will be able to receive a wider variation of signal, as indicated by the considerable discrepancy between the single and dual coils.

When the stimulus frequency reaches about 10^4 Hz, the probe's response to the same stimulus frequency results in different inductance. This indicates that the probe's response is changing from inductive to capacitive. Capacitive reactance must be avoided to acquire a safe measurement. The ideal probe can only respond inductively. Capacitive reactance will result in discontinued magnetic flux because of the nature of capacitance, which stores energy. From the experiment, a safe measurement can be acquired when the frequency stimulus is below 10^5 Hz. When the stimulus frequency is 100 Hz, or the lowest limit, the probe is unable to deliver the signal because the stimulus frequency is too low to generate proper inductance to the target or the nominal of the mutual inductance between the probe and the target is very small, and the probe cannot work properly [28].

Since the stimulus frequency for safe measurement has been obtained, the stimulus frequency that will be used for the ECT study must be determined. Udpa et al. dictate that a safe measurement can be done at least at one-tenth of the probe's resonant frequency [29]. When the probe operates at its resonant frequency, the injected signal will mask and decay the signal to be detected, interfering with the measurement. Based on the frequency test result, the 50 kHz stimulus signal will be used in the ECT to avoid the resonance frequency. The result of the FEM-based simulation is shown in Fig 10 to obtain the mapping of the magnetic flux distribution in the probe. The parameters used to model the simulation are an axisymmetric coaxial multi-coil with a homogenous multi-turn and an injection frequency set to 50 kHz. The other parameters are listed in Table 3.

TABLE III
THE PARAMETERS USED TO MODEL THE SIMULATION BASED ON THE
EXPERIMENT'S RESULTS

Coil	Parameters	Nominal	Unit
Injection	Inductance, L_0	4.3	mH
	Resistance	1.7	Ω
	Capacitance	97	pF
Detection	Inductance, L_0	15	μ H
	Resistance	2	Ω
	Capacitance	25	pF
	Coil outer radius	25	mm

The FEA simulation was also performed to confirm the probe's safe measurement. The goal of this simulation was to map the probe's magnetic flux. According to the result of the safe measurement experiment, the stimulus frequency used for the simulation is 50 kHz. The simulation begins with building the probe's geometry, defining the material properties, and determining the model, which is Ampere's law for stationary magnetic in a time-varying signal.

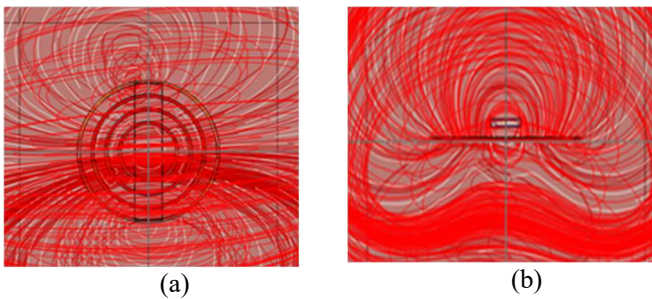


Fig. 11 The result of the FEM simulation to obtain the mapping of the magnetic flux (a) x-y view and (b) y-z view

From the simulation shown in Fig 11, we can see that at the corresponding frequency, 50 kHz, the distribution of the magnetic flux in the injection coil or injection stripe is parallel without any discontinuation. The same parallel path found in the whole geometry of the detection coil indicates that the detection process will be successful when the target is injected in the 50 kHz stimulus frequency.

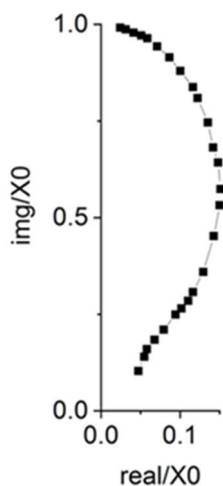


Fig. 12 Lift-off diagram of the probe

Fig. 12 above shows the result of the probe's lift-off experiment. From the lift-off diagram result, we can see that

when the probe has a 0 mm lift-off, the ratio of the imaginary component of the impedance to the probe when it is in free air is 0.103, and the real component of the impedance to the probe when it is in free air is 0.0473. When the lift-off is increased, the reactance and the resistance also increase. Finally, a similar condition as when the probe is in free air is reached when the impedance is $Z = 0 + j1$ where the fundamental component is zero, and the imaginary component is 1. This state means that the probe is no longer in contact with the conductive target [30]. This result is beneficial when the experiment uses various lift-offs. However, in this study, the lift-off experiment is used to acquire the probe's impedance when the probe assesses the target without cracking at the determined stimulus frequency, i.e., 50 kHz, and the lift-off is 0 mm. From the experiment, the probe's impedance when free from the conductive target is at 3.66 mm lift-off.

From the lift-off diagram, we can also see that the welded joint contributes to the change in conductivity of the non-magnetic base plate SS 316. The welding process significantly changes the testpiece's conductivity, making it magnetic. As shown in Fig. 12, the plot moves up counterclockwise as the lift-off increases, indicating that the target is magnetic. The base metal, SS 316, which is non-magnetic, becomes magnetic because of the welding process, which involves heat and material addition to the testpiece.

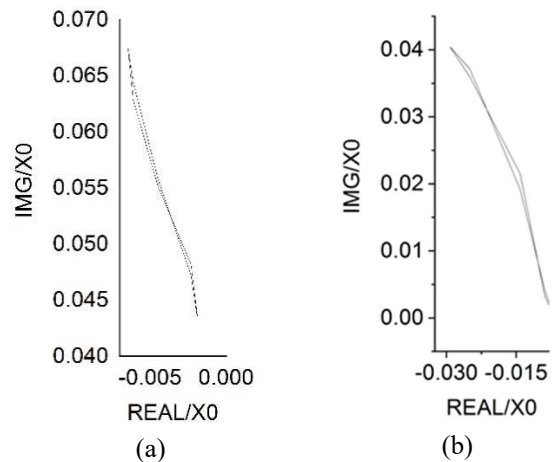


Fig. 13 The impedance diagram of the ECT (a) 1 mm crack (b) 0.5 mm crack

The impedance diagram for ECT is as shown in Fig. 13 above. As mentioned in the lift-off diagram section, the non-magnetic SS316 base metal welded joint is magnetic. The impedance diagram shows that when the probe moves towards the crack, the conductivity of the probe decreases, the reactance increases, and the resistance decreases. It indicates the decrease of the real part, or resistance, and the increase of the imaginary part, or inductive reactance. A sign of a crack in the vicinity of the probe. On the contrary, when the probe moves farther from the crack, the conductivity increases, the reactance decreases, and the resistance increases, causing the path to move clockwise. The 1 mm crack, which is larger than the previous one, emphasizes the effect almost significantly. On a 1 mm crack that leaves only 1.25 mm thick of the plate (the thickness of the target is 2.25 mm), when the probe is near the crack, the impedance is almost the same as when the probe is in the air.

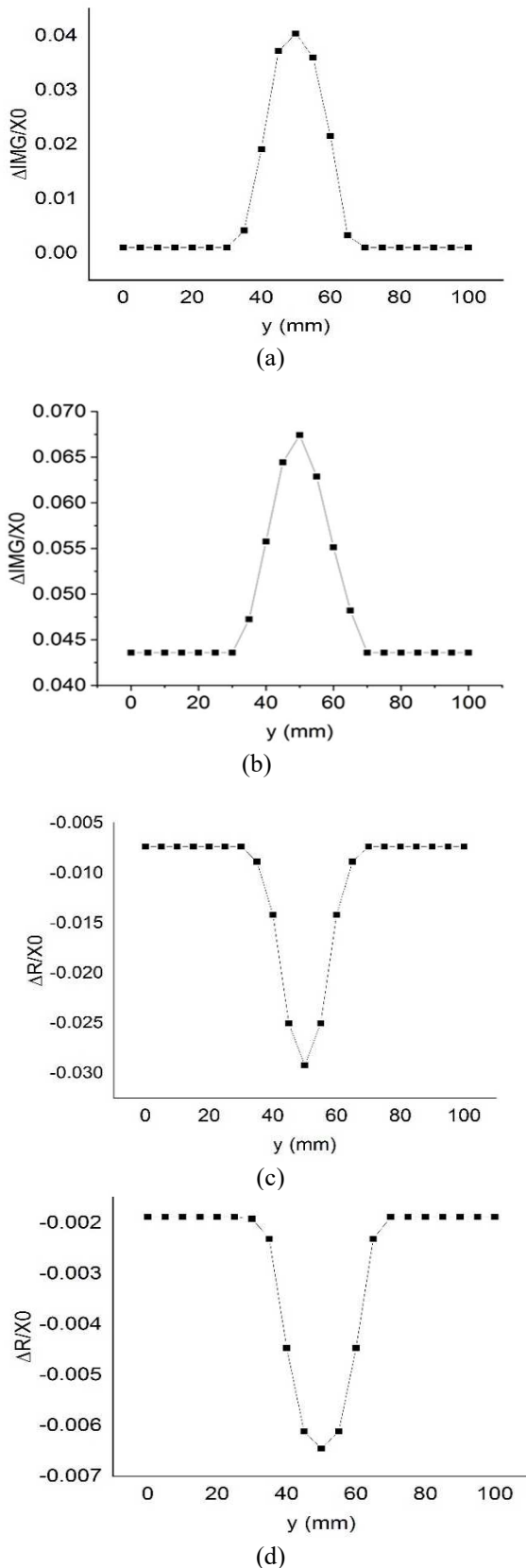


Fig. 14 The impedance of the probe versus the position of the probe (a) imaginary part of 1 mm crack (b), imaginary part of 0.5 mm crack (c) real part of 1 mm crack, and (d) real part of 0.5 mm crack.

To confirm the results of the impedance diagram, Fig. 14 shows the impedance change relative to the probe's movement along the testpiece. These figures show that the reactance will

increase, and the resistance will decrease as the probe is near the crack. 1 mm crack yields higher inductance and lower resistance than the 0.5 mm crack. In the 1 mm crack, increasing the inductance begins at 40 mm, while in the 0.5 mm crack, the effect begins to occur at 45 mm. The bigger the crack, the earlier the changes in impedance will happen compared to the more minor crack. The change in the real part, or resistance, shows the same pattern as the changes in the imaginary part. Resistance in a 1 mm crack begins to alter at 40 mm and 0.5 mm at 45 mm.

After passing the location of the crack, the real part and the imaginary part change back to their initial values. 1 mm crack changes after 60 mm and 70 mm for the imaginary and real parts of the impedance. In the 0.5 mm crack, the changes begin at 65 mm on both the real part and the imaginary part. It can be seen that the 0.5 mm crack yields fewer changes in the inductive reactance results compared to the 1 mm crack. This is because the 0.5 mm crack has a smaller air volume, causing a smaller resonance than the 1 mm crack, which contains more air. Resonance causing 1 mm crack has a higher amplitude than the 0.5 mm crack. So the larger the crack, the greater the amplitude [16].

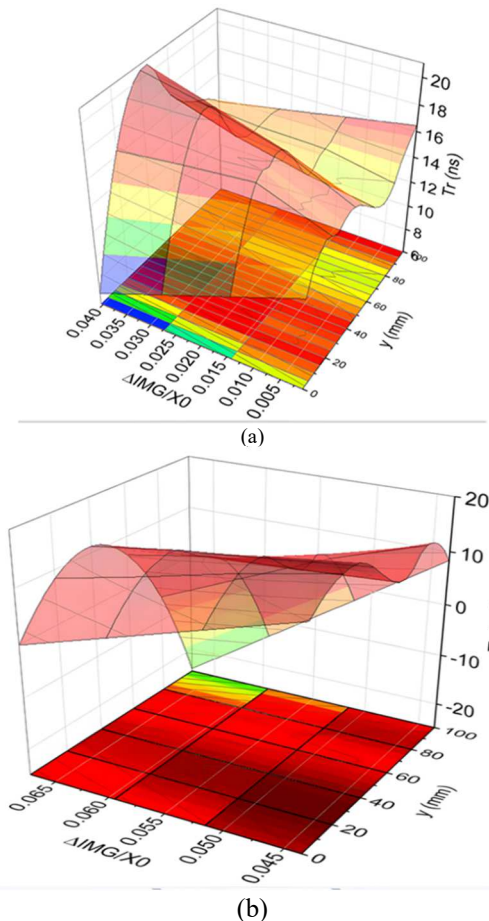


Fig. 15 Plot of rise time (Tr) as the function of the system's response to the imaginary part of the impedance and the position of the probe (a) 1 mm crack (b) 0.5 mm crack

Fig. 15. shows the relationship between inductive reactance, or the imaginary part of the impedance, the rise time, and the probe's position. Rise time (Tr) represents the result of the system's response. It states the time required for

the response due to a step input to reach its final value, which is acquired from the system response analysis. From Fig. 15, we can see that the rise time decreases as the probe approaches the location of the crack. It means the time required to reach its final value is faster, indicating a quicker steady state. The response is less oscillatory as the steady state is reached faster. This has to do with conductivity. When no crack is present, conductivity is high, producing more eddy and countercurrent [31]. It takes more time for the response to reach its final value because it becomes more oscillatory. The presence of cracks, which means less conductivity, reduces the effect of conductivity, causing less oscillation and a faster rise time.

As the inductive reactance increases, the rise time decreases, indicating that as the inductive reactance increases, the final value of the response is faster. The previous result can confirm this: when the crack is present, the inductive reactance, or the imaginary part of the impedance, will increase. The system's response analysis indicates that the presence of the crack will decrease the rise time.

If observed further, the rise time alters even though the probe position is still some distance from the crack location and does not return to its original position when the probe moves away from the crack location. From this result, we can conclude that by applying the system response analysis, the occurrence of magnetic power storage or magnetic reminiscence in the system can be detected [32]. The larger the crack size, the smaller this effect becomes due to the decrease in conductivity [33].

IV. CONCLUSION

In this study, system response analysis is applied and compared to the classical ECT. It has been shown that the welding process changed the conductivity by involving a heat process and material addition to the testpiece. The fabricated probe had successfully assessed the presence of the cracks. The results of the system response analysis agreed with the classical ECT. From the system's response results, magnetic reminiscence occurs during the assessment, which is affected by the presence and size of the cracks. The magnetic reminiscence found in this study can be useful to investigate the presence of the crack and should be studied further.

ACKNOWLEDGMENT

We acknowledge the financial support from Universitas Muhammadiyah Semarang that helped us to present the study.

REFERENCES

- [1] S. Patra, G. Singh, M. Mandal, R. Chakraborty, and K. S. Arora, "Non-destructive evaluation and corrosion study of magnetic pulse welded Al and low C steel joints," *Mater. Chem. Phys.*, vol. 309, p. 128315, 2023, doi: 10.1016/j.matchemphys.2023.128315.
- [2] S. Gang and H. Minghui, "Signal Processing and Defect Characterization of Pulsed Eddy Current Testing Based on Cross-Correlation," *Procedia Comput. Sci.*, vol. 208, pp. 300–309, 2022, doi: 10.1016/j.procs.2022.10.043.
- [3] A. Aoukili and A. Khamlichi, "Modeling an Eddy-Current Probe for Damage Detection of Surface Cracks in Metallic Parts," *Procedia Technol.*, vol. 22, pp. 527–534, 2016, doi: 10.1016/j.protcy.2016.01.112.
- [4] M. Mussatayev, Q. Yi, M. Fitzgerald, V. K. Maes, P. Wilcox, and R. Hughes, "Directional eddy current probe configuration for in-line detection of out-of-plane wrinkles," *Compos. Part B Eng.*, vol. 268, p. 111048, 2024, doi: 10.1016/j.compositesb.2023.111048.
- [5] Z. D. Wang, Y. Gu, and Y. S. Wang, "A review of three magnetic NDT technologies," *J. Magn. Magn. Mater.*, vol. 324, no. 4, pp. 382–388, 2012, doi: 10.1016/j.jmmm.2011.08.048.
- [6] L. Q. Trung, N. Kasai, K. Sekino, and N. C. Hanh, "The effect of eddy current probe configurations on crack signal magnitude: Consideration of excitation coil direction," *Sensors Actuators A Phys.*, vol. 358, p. 114437, 2023, doi: 10.1016/j.sna.2023.114437.
- [7] Q. Ma, G. Y. Tian, B. Gao, X. Zhao, G. Ru, and H. Li, "Lift-off suppression based on combination of bridge and transformer signal conditionings of eddy current testing," *NDTE Int.*, vol. 132, p. 102724, 2022, doi: 10.1016/j.ndteint.2022.102724.
- [8] T. P. Theodoulidis and E. E. Kriezis, "Impedance evaluation of rectangular coils for eddy current testing of planar media," *NDTE Int.*, vol. 35, no. 6, pp. 407–414, 2002, doi: 10.1016/S0963-8695(02)00008-7.
- [9] L. U. Daura, G. Tian, Q. Yi, and A. Sophian, "Wireless power transfer-based eddy current non-destructive testing using a flexible printed coil array Subject Areas :," 2020.
- [10] L. Barbato, N. Poulakis, A. Tamburrino, T. Theodoulidis, and S. Ventre, "Solution and Extension of a New Benchmark Problem for Eddy-Current Nondestructive Testing," *IEEE Trans. Magn.*, vol. 51, no. 7, 2015, doi: 10.1109/TMAG.2015.2406765.
- [11] F. Xie, X. Wu, H. Zhang, and X. Zhang, "Research on pulsed eddy current automatic detection technology for weld defects of pressure vessel cylinder," *Measurement*, vol. 176, p. 109081, 2021, doi:10.1016/j.measurement.2021.109081.
- [12] N. Yusa, E. Machida, L. Janousek, M. Rebican, Z. Chen, and K. Miya, "Application of eddy current inversion technique to the sizing of defects in Inconel welds with rough surfaces," vol. 235, pp. 1469–1480, 2005, doi: 10.1016/j.nucengdes.2005.01.005.
- [13] C. Chen and C. Hung, "Improving LCC Series-Based Wireless Power Transfer System Output Power at High Temperature," 2021.
- [14] Z. H. Guo and S. E. Dong, "Receiver power allocation and transmitter power control analysis for multiple-receiver wireless power transfer systems," *J. Electron. Sci. Technol.*, vol. 17, no. 4, p. 100009, 2019, doi: 10.1016/j.jnlest.2020.100009.
- [15] W. Zhong, D. Xu, R. Shu, Y. Hui, and B. Distance, *Wireless Power Transfer between distance and efficiency*. 2020.
- [16] C. G. Camerini *et al.*, "Correlation of eddy current signals obtained from EDM notches and fatigue cracks," *J. Mater. Res. Technol.*, vol. 8, no. 5, pp. 4843–4848, 2019, doi: 10.1016/j.jmrt.2019.08.031.
- [17] D. Wu, W. Chen, J. Yang, and F. Yang, "Self-resonance eddy-current testing method in noncontact detection of carbon fiber reinforced plastics," *Compos. Struct.*, vol. 259, p. 113247, 2021, doi:10.1016/j.compstruct.2020.113247.
- [18] I. I. Abdalla, T. Ibrahim, N. Perumal, and N. M. Nor, "Minimization of Eddy-Current Loss in a Permanent-Magnet Tubular Linear Motor," vol. 7, no. 3, pp. 964–970, 2017, doi: 10.18517/ijaseit.7.3.2280.
- [19] N. S. Nise, "Control System Engineering (8th edition)," Wiley, p. 1726, 2019.
- [20] S. Viqar, A. Ahmad, S. Kirmani, Y. Rafat, M. R. Hussan, and M. S. Alam, "Modelling, simulation and hardware analysis of misalignment and compensation topologies of wireless power transfer for electric vehicle charging application," *Sustain. Energy, Grids Networks*, vol. 38, p. 101285, 2024, doi: 10.1016/j.segan.2024.101285.
- [21] S. H. Ahmed and I. Ahmad, "Optimal wireless power transfer to hybrid energy storage system for electric vehicles: A comparative analysis of machine learning-based model-free controllers," *J. Energy Storage*, vol. 75, p. 109534, 2024, doi: 10.1016/j.est.2023.109534.
- [22] F. Xu and H. Huang, "Frequency selection for underwater wireless power transfer based on the analysis of eddy current loss," *AEU - Int. J. Electron. Commun.*, vol. 163, p. 154618, 2023, doi:10.1016/j.aeue.2023.154618.
- [23] Y. Yu and P. Du, "Two approaches to coil impedance calculation of eddy current sensor," *Proc. Inst. Mech. Eng. Part C J. Mech. Eng. Sci.*, vol. 222, no. 3, pp. 507–515, 2008, doi: 10.1243/09544062JMES395.
- [24] M. S. Luloff, J. Morelli, and T. W. Krause, "Examination of Dodd and Deeds solutions for a transmit-receive eddy current probe above a layered planar structure," *AIP Conf. Proc.*, vol. 1806, 2017, doi:10.1063/1.4974682.
- [25] M. S. Luloff, J. Morelli, T. W. Krause, M. S. Luloff, J. Morelli, and T. W. Krause, "Examination of Dodd and Deeds solutions for a transmit-receive eddy current probe above a layered planar structure Examination of Dodd and Deeds Solutions for a Transmit-Receive Eddy Current Probe above a Layered Planar Structure," vol. 110004, no. February, 2017, doi: 10.1063/1.4974682.

- [26] A. C. Lahrech *et al.*, “Development of an axial rotating magnetic field multi-coil eddy current sensor for electromagnetic characterization of stratified CFRP materials,” *NDT E Int.*, vol. 126, p. 102589, 2022, doi:10.1016/j.ndteint.2021.102589.
- [27] S. She, Y. Chen, Y. He, Z. Zhou, and X. Zou, “Optimal design of remote field eddy current testing probe for ferromagnetic pipeline inspection,” *Measurement*, vol. 168, p. 108306, 2021, doi:10.1016/j.measurement.2020.108306.
- [28] M. Lu, X. Meng, R. Huang, L. Chen, A. Peyton, and W. Yin, “Lift-off invariant inductance of steels in multi-frequency eddy-current testing,” *NDT E Int.*, vol. 121, p. 102458, 2021, doi:10.1016/j.ndteint.2021.102458.
- [29] Navair, “Eddy Current Inspection Method,” *NDT supply*, vol. TM1-1500-3, no. TO 33B-1-1, 2009.
- [30] J. Li, X. Wu, Q. Zhang, and P. Sun, “Measurement of lift-off using the relative variation of magnetic flux in pulsed eddy current testing,” *NDT E Int.*, vol. 75, pp. 57–64, 2015, doi:10.1016/j.ndteint.2015.06.008.
- [31] M. Mirzaei, P. Ripka, A. Chirtsov, and V. Grim, “Journal of Magnetism and Magnetic Materials Eddy current speed sensor with magnetic shielding,” vol. 502, no. February, 2020.
- [32] G. Yilmaz and C. Dehollain, *Wireless Power Transfer*. 2017. doi:10.1007/978-3-319-49337-4_3.
- [33] M. Coramik and Y. Ege, “Discontinuity inspection in pipelines: A comparison review,” *Meas. J. Int. Meas. Confed.*, vol. 111, no. July, pp. 359–373, 2017, doi: 10.1016/j.measurement.2017.07.058.